Materials Research Bulletin 93 (2017) 47–55

Contents lists available at ScienceDirect

Materials Research Bulletin

journal homepage: www.elsevier.com/locate/matresbu

Optical and gas-sensing properties, and electronic structure of the mixed-phase $CaCu_3Ti_4O_{12}/CaTiO_3$ composites

L.H. Oliveira[a], M.A. Ramírez[b], M.A. Ponce[c], L.A. Ramajo[c], A.R. Albuquerque[d], J.R. Sambrano[e], E. Longo[a], M.S. Castro[c], F.A. La Porta[f,*]

[a] State University of São Paulo, Chemistry Institute, rua Prof. Francisco Degni 55, 14800-905, Araraquara, SP, Brazil
[b] State University of São Paulo, Engeenering Collegue of Guaratinguetá, rua Ariberto Pereira da Cunha, 12516-410, Guaratinguetá, SP, Brazil
[c] University of Mar del Plata, Institute of Materials Science and Technology, J.B. Justo 4302, Mar del Plata, Buenos Aires B7608FDQ, Argentina
[d] Federal Institute of Education, Science and Technology of Sertão Pernambucano, 56400-000 Floresta, PE, Brazil
[e] Modeling and Molecular Simulations Group, São Paulo State University, UNESP, 17033-360 Bauru, SP, Brazil
[f] Federal Technological University of Paraná, Laboratory of Nanotechnology and Computational Chemistry, avenida dos Pioneiros 3131, 86036-370, Londrina, PR, Brazil

ARTICLE INFO

Article history:
Received 9 January 2017
Received in revised form 7 April 2017
Accepted 22 April 2017
Available online 24 April 2017

Keywords:
DFT
Gas sensing
Photoluminescence
CCTO/CTO composites
Screen-printing technique

ABSTRACT

Combined experimental and theoretical investigations were conducted on the electronic structure, as well as the optical and gas-sensing properties of mixed-phase $CaCu_3Ti_4O_{12}/CaTiO_3$ (CCTO/CTO) composites, which were synthesized by a solid-state reaction using various milling durations. Our results revealed that these CCTO/CTO composites have a broad photoluminescence (PL) emission band located at 450 nm, which is strongly influenced by the milling process duration. Scanning electron microscopy images confirmed that the use of longer milling durations favored the formation of pores and increased the active surface area of the CCTO/CTO thick films. The thick films were prepared using the screen-printing technique, and hence, could be structured for gas-sensing applications. Our theoretical findings may further elucidate the electronic structure associated with the interfacial band alignment (type I-straddling gap) of the CCTO/CTO composite systems.

1. Introduction

During the last decade, the dielectric properties of $ACu_3Ti_4O_{12}$ (with A = metallic ions) perovskites has gained much attention due to its extraordinarily high and almost temperature-independent dielectric values [1–11]. The $CaCu_3Ti_4O_{12}$ (CCTO) material has a body-centered cubic structure with a space group of Im-3. In this crystalline structure, one-quarter of the A sites are occupied by Ca atoms coordinated to twelve oxygen atoms, while three-quarters of the A sites are occupied by Cu atoms coordinated to four oxygen atoms. Ti atoms are located at the B sites, which are coordinated to six oxygen atoms in an octahedral configuration [2–4]. Compared to other perovskites (e.g., $BaTiO_3$, $K_{1/2}Na_{1/2}NbO_3$, $BiTiO_3$, and so on), at 100–400 K and above 1 MHz, this material has a high dielectric permittivity value (~10,000ε_0). Owing to their outstanding dielectric properties, CCTO materials can be used in microe lectronic devices. Chung et al. [5] has also determined that this material exhibits strong non-linear current–voltage behavior, which enhances its application for varistor devices.

The origin of the dielectric properties of CCTO materials has been the subject of several studies, and their remarkable properties have been attributed to intrinsic mechanisms [6,7]. Incidentally, the high dielectric permittivity of the material has been ascribed to local structural polarization associated with the displacement of Ti^{4+} ions from the symmetric center. However, other researchers have attributed the electrical behavior of the CCTO system to extrinsic mechanisms [8–11]. For instance, Sinclair et al. [10] determined that CCTO is composed of semiconductor grains and an isolated grain boundary; this heterogeneity would be responsible for the formation of internal capacitive barrier layers, which would influence the dielectric permittivity values of the material. In addition, Fang et al. [11] suggested that internal domains exist inside the CCTO grains; this may result in enhancement of the

* Corresponding author.
E-mail addresses: felipe_laporta@yahoo.com, felipelaporta@utfpr.edu.br (F.A. La Porta).
URL: http://mailto:felipe_laporta@yahoo.com.br (F.A. La Porta)

http://dx.doi.org/10.1016/j.materresbull.2017.04.037
0025-5408/

dielectric permittivity of the CCTO due to the contribution of the individual grains.

The physical and chemical properties of CCTO materials can be influenced by the Ca/Cu ratio [12–16]. Consequently, the dielectric permittivity, resistivity, and density of CCTO materials are closely related to the segregation of CuO at the grain boundaries [12,13]. For instance, Kim et al. [14] determined that enhanced permittivity values were obtained for Cu-rich CCTO samples. In principle, excess CuO, which is not incorporated into the CCTO system, can increase the amount of liquid phase at the grain boundary regions. In contrast, when Ca atoms initially occupy Cu sites, which results in a Ca-rich CCTO solid solution due to differences in the atomic radii of the Ca^{2+} and Cu^{2+} ions, the solubility limit of Ca atoms in the CCTO system is low; therefore, the excess of Ca atoms can, in principle, favor the formation of $CaTiO_3$ (CTO) as a secondary phase [15]. In addition, recent studies have reported that owing to the stoichiometry of CCTO systems, the formation of a Ca-rich CCTO solid solution is energetically more favorable than the formation of a Cu-rich CCTO solid solution [17].

Many researchers have studied the fabrication of various forms of CCTO and CTO materials using numerous processing methods, such as metal-organic chemical deposition [18–20], sol-gel [21,22], pulsed laser deposition [23], pressure-assisted thermal annealing [24], and so on. In addition, it is widely recognized that these techniques, when applied for the preparation of CCTO and/or CTO films, in particular, lead to the formation of materials with irregular grain sizes and rough surfaces. More recently, to improve the performance of such materials for potential application in integrated circuit devices, the screen-printing technique has been used to fabricate thick films. This technique results in the production of crack-free thick films with a highly porous structure compared with those produced with other deposition techniques [25–27].

In contrast, recent studies have reported that the chemical and physical properties of mixed-phase CTO/CTO composite systems are significantly influenced by their formation process [28–30]. In theory, the formation process can lead to changes in the electronic structure properties due to the adjustment of the relative band alignments of both materials, which primarily occurs at the interface regions [31]. Consequently, composites consisting of mixed-phases have huge potential for a wide variety of technological applications. Recent studies have focused on the microstructure and dielectric properties of mixed-phase CCTO/CTO composites (i.e., as a function of their stoichiometry), and thus, these complex heterostructured materials may have significantly enhanced dielectric constants as well as typical non-linear coefficients [32–34]. However, despite recent advances in this field, it is important to gain a more fundamental understanding of these composites. In addition, at nanoscale sizes, the structural and electronic properties of such composites are yet to be elucidated.

In the present study, we conducted a combined experimental and theoretical investigation on the electronic structure, as well as the optical and gas-sensing properties of a CCTO/CTO composite that was synthesized by a solid-state reaction using various milling durations. These composites were characterized using X-ray diffraction (XRD), field-emission scanning electron microscopy (FE-SEM), micro-Raman (MR) spectroscopy, and volumetric gas adsorption measurements with Brunauer-Emmett-Teller (BET) analyses. The optical properties of the mixed-phase CCTO/CTO composites were evaluated using diffuse-reflectance spectroscopy in the ultraviolet–visible region (DRS/UV–vis) as well as photoluminescence (PL) measurements. To obtain thick films of these as-prepared composites, the material was deposited onto an alumina substrate using a screen-printing technique [35]. In additional, the gas-sensing response of the thick films was evaluated under air and CO atmospheres. To further understand the experimental data, the electronic band structure, vibrational modes, and projected density of states of both the CTO and CCTO materials were theoretically calculated to predict the band-alignment mechanism, and elucidate the physical and chemical behaviors of the materials at an atomic-level.

2. Experimental section

2.1. Synthesis of the CCTO/CTO composites

The CCTO/CTO composite powders were prepared using a solid-state reaction. Stoichiometric quantities of TiO_2, CuO, and $CaCO_3$ (Aldrich, 99.99%) were placed in isopropanol within a polyethylene bottle and ball-milled using zirconia balls. The compounds were milled for 24 h and 48 h to obtain powders with a small particle size, and the resultant products were denoted as CCTO/CTO_1 and CCTO/CTO_2, respectively. The alcohol subsequently evaporated, and the resultant powders were mechanically disaggregated in a mortar, sieved using a 200-mesh granular sieve, and calcined at 900 °C for 12 h in a conventional furnace, which was heated at a rate of 5 °C/min.

2.2. Characterizations

The crystallinity of the CCTO/CTO powders and thick films were verified using XRD. A Rigaku-DMax/2500PC (Japan) with Cu-Kα radiation (λ = 1.5406 Å) was operated in the 2θ ranges of 10–130° and 20–70° with a scanning rate of 0.02°/min. The morphologies of the powders and thick films were verified using a FE-SEM (JEOL JSM-6460LV microscope). The surface areas of the CCTO/CTO powders were determined by gas-adsorption volumetric measurements using BET analysis. The MR spectra of the mixed-phase CCTO/CTO powders and thick films were recorded using a Renishaw in via microscope. In particular, the MR spectra were obtained using an argon-ion laser with a wavelength of 514 nm, where the maximum output power was maintained at 50 mV; the spectra were dispersed using diffraction scattering at 2400 lines/min.

2.3. Optical properties

The DRS/UV-vis spectra of the mixed-phase CCTO/CTO composites were measured using a Cary 5G spectrophotometer. The PL emission spectra were measured using a 139 Thermal Jarrell-Ash Monospec 27 monochromator and a Hamamatsu R446 photomultiplier. A krypton-ion laser (Coherent Innova) with an exciting wavelength of 350 nm was used and a nominal output power of 200 mW was maintained. All the measurements were performed at room temperature.

2.4. Fabrication and electrical characterization of thick films

The thick films were prepared using a screen-printing method. First, silver electrodes (interdigital paths of approximately 1 mm) were deposited on a dense alumina substrate using a screen composed of polymeric resin. The silver electrodes were heated to 350 °C at a rate of 5 °C/min and maintained at this temperature for 0.5 h. To prepare the slurry, 200 mg of the CCTO/CTO (1 and 2) powders and two drops of glycerin were mixed in a mortar. The viscosity was controlled using an isopropanol solution. The slurry was deposited on the electrodes using a glass rod. To improve the film adhesion, the alumina substrates were initially calcined at 60 °C for 1 h and subsequently at 500 °C for 1 h; in both cases, a heating rate of 2 °C/min was employed.

The electrical behavior of the mixed-phase CCTO/CTO thick films was investigated using a gas chamber. The samples were

subjected to a dry air atmosphere at low pressure, and a resistance versus time curve was plotted. Following a sudden change in the atmospheric conditions, from vacuum (10–4 mmHg) to dry air (3.6 mmHg and 9.0 mmHg), the resistance was measured as a function of time at temperatures of 250–400 °C. The sensibility of the CCTO/CTO thick films in the O2 assay was calculated using a $S = R_{air}/R_{vacuum}$ ratio, where R_{air} is the constant resistance value following the injection of air, and R_{vacuum} is the resistance value prior to the injection.

For sensing measurements under CO atmosphere, the samples were exposed to vacuum conditions, and a quantity of CO was injected (3.6 mmHg); this moment was determined as the initial time (t = 0). Gas-sensing measurements were recorded until there was no variation in the resistance values. Subsequently, the sample was exposed to vacuum conditions again, and 9.0 mmHg of air was injected. When the resistance attained a stationary state, a quantity of CO ($P_{air} + P_{CO} = 20$ mmHg) was injected, and measurements were recorded until the resistance became constant. All the measurements were recorded at 390 °C.

2.5. Theoretical models and methods

The structural, vibrational, and electronic properties of the bulk-phase CCTO and CTO materials were investigated via periodic first-principles calculations within the framework of density functional theory (DFT) [35,36] using the CRYSTAL 14 package [37]. This code employs a Gaussian-type basis set (GTO) to represent Kohn–Sham orbitals in periodic systems as a linear combination of Bloch functions, which are defined in terms of the local functions (atomic orbitals).

Consistent GTO with triple-zeta valence with polarization quality (TZVP) were constructed for the solid-state calculations [38]; these were used for all atoms and described by the all-electron basis set (s-p-d-f), namely Ti and Cu: 842111-6311-411-1; Ca: 842111-6311-1, and O: 6211-411-1.

The CTO is orthorhombic (Pbnm – lattice parameter a = 5.3796 Å, b = 5.4423 Å, c = 7.6401 Å) with closed shell system, and was treated under restricted formalism. The CCTO is cubic (Im-3–lattice parameter a = 7.391 Å) and has an open shell system because of the three Cu ($[Ar]3d^{10}4s^{1}$) atoms in the unit cell. This system was treated under unrestricted Hamiltonian formalism within the high-spin ferromagnetic solution. Owing to the strong electronic correlation in systems such as CCTO, we used the global hybrid model, PBE0, and range-separated hybrid functionals, HSE06, to mitigate self-interaction error.

The level of calculation accuracy for the Coulomb and exchange series was controlled by five thresholds set to $10^{-8}, 10^{-8}, 10^{-8}, 10^{-8}, 10^{-16}$ (for more details see CRYSTAL Manual [37]). Diagonalization of the Fock matrix was performed using a shrinking factor (Pack–Monkhorst and Gilat net), which was set to 6, corresponding to 18 independent k-points in the irreducible part of the Brillouin-zone integration of the CCTO, and 64 k-points in the case of the CTO. The atomic positions of all the atoms in each of the models were fully relaxed until the largest component of the ionic forces attained a value of 3×10^{-4} eV/Å. The electronic band structure and its density of states (DOS) were analyzed using the Properties14 routine of the CRYSTAL code; to optimize the data, we employed the same k-point sampling as that used during the diagonalization of the Fock matrix.

In particular, the vibrational frequencies (infrared and Raman spectroscopy) at the Γ point were computed within the harmonic approximation by diagonalizing the mass-weighted Hessian matrix. The convergence threshold was set to 10^{-7} and 10^{-10} Ha to perform SCF energy calculations for the optimization and vibrational frequencies, respectively.

3. Results and discussion

Fig. 1(a) depicts the XRD patterns, recorded at room temperature, of both samples prepared using the solid-state reaction. It is evident that all the XRD patterns can be indexed to the cubic structure of the CCTO (with a space group of Im-3) and the orthorhombic structure of the CTO (with a space group of Pbnm). These results confirm that mixed-phase CCTO/CTO composites were obtained, and are in good agreement with the respective Inorganic Crystal Structure Database cards (ICSD card numbers 95–714 and 74–212), as shown in Fig. 1 (a). In addition, similar results were obtained for the thick films (see Fig. 1(b)). Moreover, no diffraction peaks associated with the alumina substrate were observed during the XRD analysis of the thick films. The XRD results are in agreement with those of previous studies [29,33,34], and indicate that a high degree of structural order and crystallinity exist at long-range. Furthermore, we also analyze the crystallite sizes of the CCTO/CTO powders, as well as for the thick films as-prepared, were calculated from the full-width at half maxima (FWHM) of the (220) peak at $\sim 2\theta = 33°$ corresponding to CCTO phase and (121) peak at $\sim 2\theta = 34°$ corresponding to CTO phase using Scherer's method [39].

The crystallite size values found for the CCTO/CTO powders and thick films (given in parentheses) calculated from the (220) peak varies from 422.13 (398.36) nm to 184.05 (196.93) nm, while for the (121) peak varies from 66.31 (70.32) nm to 64.92 (73.86) nm; respectively, as a function of the milling stages. This observed differences for both cases could originate from the higher lattice distortions caused by residual stresses induced by 24 or 48 h at milling process, i.e., due to preparation conditions in solid state reaction method including heat treatment temperature, processing time and stages of grinding, as well as, in the case of thick films,

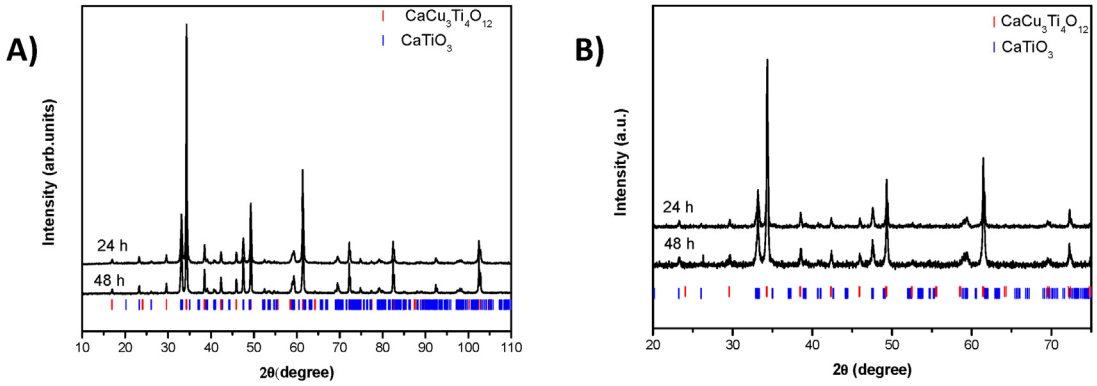

Fig. 1. XRD patterns of the CCTO/CTO (a) powders and (b) thick films.

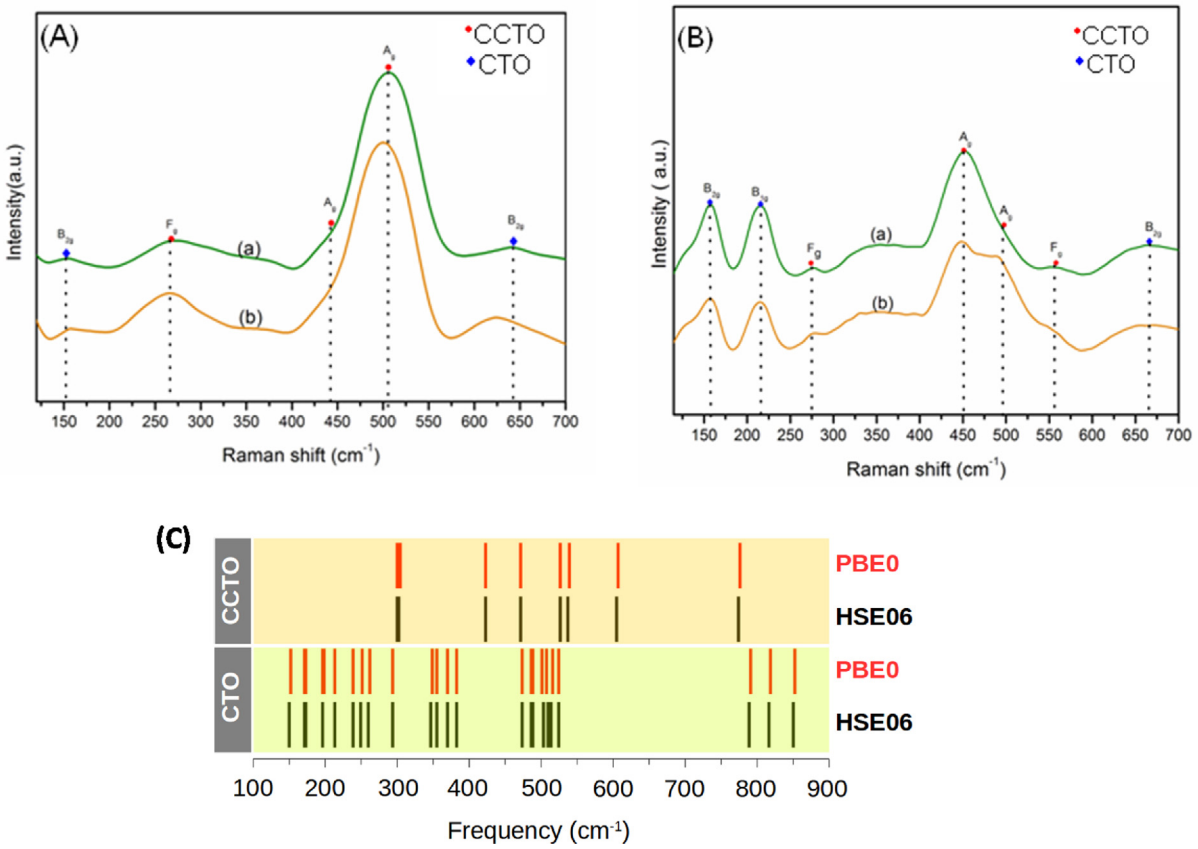

Fig. 2. Experimental MR spectra of the CCTO/CTO (a) powders and (b) thick films. (c) Raman frequencies of CCTO and CTO at the PBE0 and HSE06 theoretical levels.

the large lattice mismatch and a large difference in thermal expansion coefficients between CCTO/CTO on alumina substrates (e.g., which causes a residual stress in deposited CCTO/CTO thick films).

Fig. 2(a–b) show the MR spectra of the powders and thick films consisting of the mixed-phase CCTO/CTO composite systems, respectively. The analysis of the MR spectra of the CCTO/CTO composite powders, shown in Fig. 2(a–b), reveals three Raman-active modes (i.e., $1F_g$ and $2A_g$) that are characteristic of octahedral [TiO_6] cluster rotation-like behavior in the cubic structure of the CCTO phase as well as three other Raman-active modes (i.e., $2B_{2g}$ and $1B_{1g}$) that are related to the [Ti—O—Ti] anti-symmetric stretching mode. In addition, [O—Ti—O] bending vibration modes, caused by the tilting phenomenon between adjacent octahedral [TiO_6] clusters in the orthorhombic CTO phase, were also revealed [40–43]. Considering these experimental results, the vibrational modes and their corresponding frequencies were theoretically calculated from the optimized bulk structure of both the CCTO and CTO materials. No imaginary frequencies, which indicate the presence of structures in local or global minima, were found. The bulk CCTO and CTO structures have 60 modes. Owing to the cubic symmetry of the CCTO, the F-modes are triple degenerated and the E-modes are double degenerated, resulting in irreducible representations with just 24 modes, as shown in the following equations:

$$\textbf{CTO: } \Gamma = (8A_u)_{silent} + (8B_{1u} + 10B_{2u} + 10B_{3u})_{IR} + (7A_g + 7B_{1g} + 5B_{2g} + 5B_{3g})_{Raman} \quad (1)$$

$$\textbf{CCTO: } \Gamma = (2E_u + 2A_u)_{silent} + (12F_u)_{IR} + (4F_g + 2E_g + 2A_g)_{Raman} \quad (2)$$

The representations with the subscript 'u' are Infrared-active, while the g-modes are Raman-active; the A_u- and E_u-modes are silent in the case of both oxides. The positions of the optical Raman-active modes obtained from the DFT calculations are shown in Fig. 2(c). A comparison of both the PBE0 and HSE06 theoretical levels predicted the positions of the modes in the same region of the spectra; these results correlated well with the experimental results (for more details, see the Supplementary information).

In addition, it is clear that the MR spectra of the powder and thick-film CCTO/CTO_2 systems are rather different to those of the corresponding samples. In the case of the CCTO/CTO_2 powder, the difference can be noted by the disappearance of the Raman mode at 441 cm^{-1} and the displacement of the Raman mode at 641 cm^{-1}. However, in the case of the CCTO/CTO_2 thick film, this difference is noted by the appearance of the Raman-active mode at 501 cm^{-1}. Each of these Raman-active modes are related to the rotation-like mode of the [TiO_6] clusters. Moreover, the observed changes in the Raman-active modes of the CCTO/CTO_2 systems also indicate that the structural defects induced by the milling stages can modify the bending vibration of the [Ti-O] linkages in the CCTO/CTO crystalline structure. In additional, the MR results correlate well with those of the XRD pattern analysis, and hence also reveal that short-range structural organization exists in the mixed-phase CCTO/CTO composite systems.

Fig. 3(a–b) illustrate the FE-SEM micrographs of the powder and thick-film mixed-phase CCTO/CTO composite systems, respectively. The CCTO/CTO_1 powder has a surface area of 8.1 $m^2 g^{-1}$ and possesses large particles. However, the CCTO/CTO_1 thick film possesses loose particles with no points of contact; the initial stage of sintering cannot be initiated, which indicates that there is almost no connectivity between the particles (see Fig. 3(c)). For

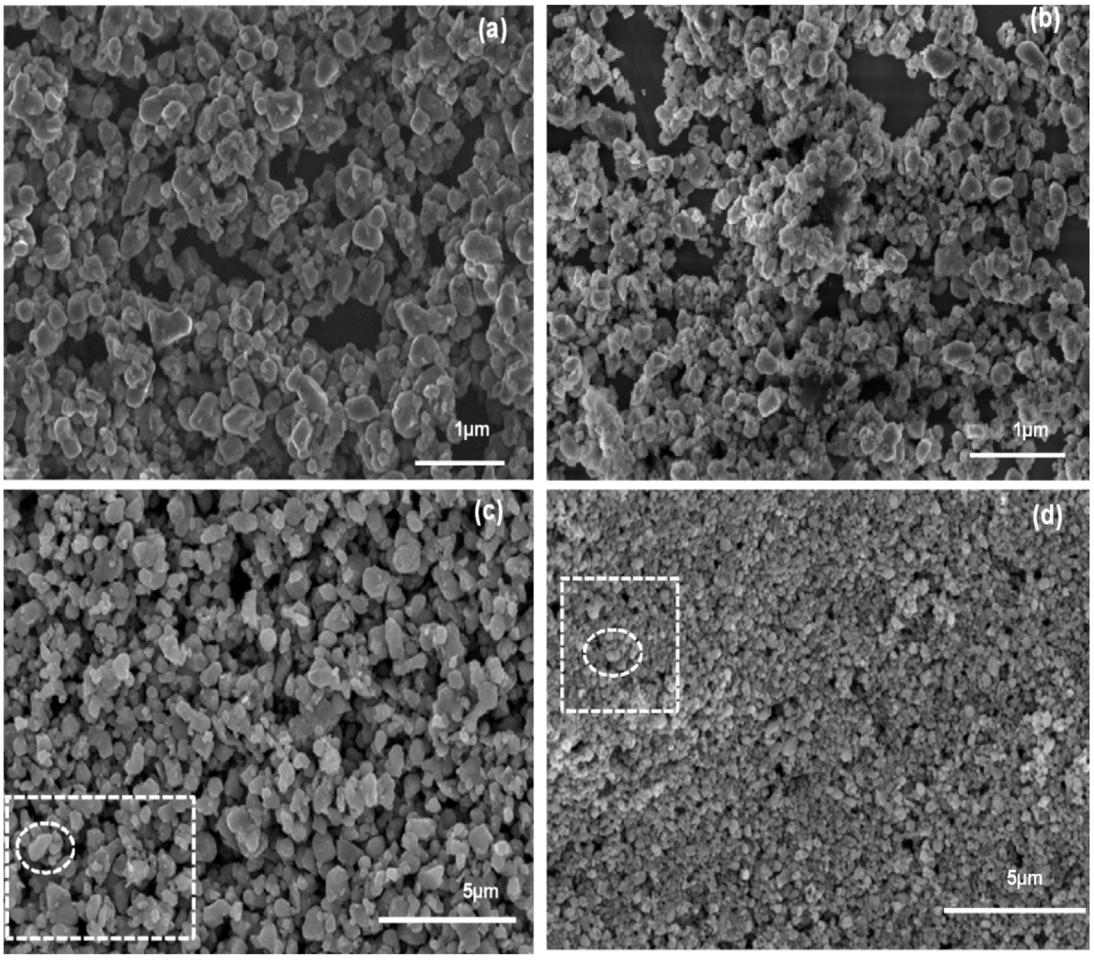

Fig. 3. SEM images of the CCTO/CTO_1(a) and CCTO/CTO_2(b) powders, CCTO/CTO_1 (c), and CCTO/CTO_2(d) thick films.

comparison, the CCTO/CTO_2 powder has a large surface area of 18.2 $m^2 g^{-1}$. The heat treatment increases the number of contact points between the particles in this sample; consequently, it is energetically feasible that these particles join to form many aggregates with greater connectivity (see Fig. 3(d)). The preliminary results show that in the case of the CCTO/CTO_2 film, there is a greater degree of connectivity between the particles compared to that of the CCTO/CTO_1 film.

Fig. 4(a) illustrates the DRS/UV-vis spectra of the CCTO/CTO_1 and CCTO/CTO_2 powders, which were employed to determine the band-gap values (E_{gap}) of these composites using the Tauc procedure [44]. In particular, it is well known that the CCTO/

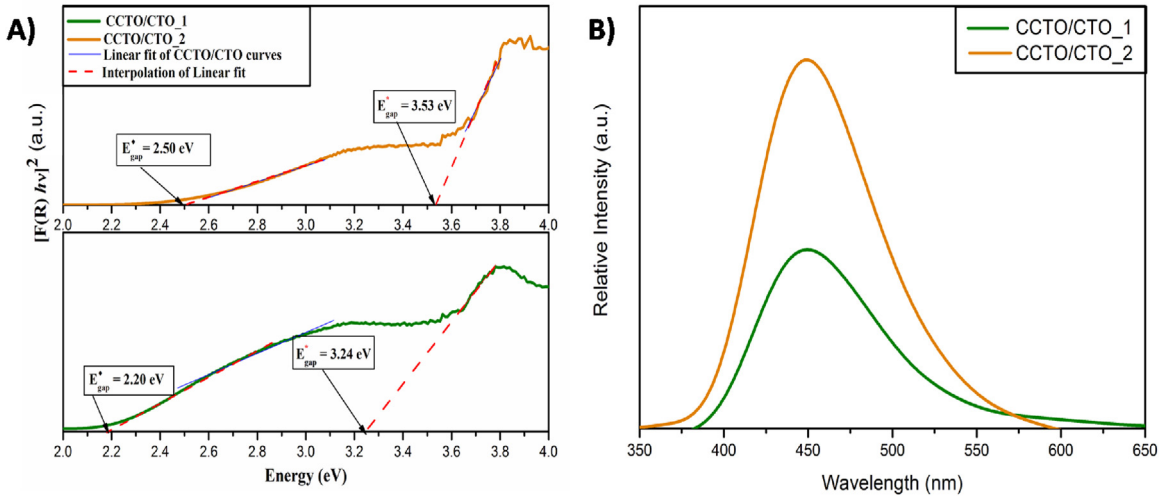

Fig. 4. (a) UV–vis spectra and (b) PL emission spectral of the CCTO/CTO powders prepared by solid state reaction.

CTO composite systems have a direct E_{gap} energy, which corroborates our theoretical results. These results indicate that two different direct allowed transitions were determined for the materials; these can be assigned to each phase of this system, which corresponds with both the XRD and MR results. From the PBE0 and HSE06 theoretical approaches, it could be determined that the band gap of the CCTO was smaller than that of the CTO, where the Fermi level at T = 0 had almost degenerated. Therefore, it is expected that two possible effective band gaps will exist, which are provided relatively equally from the separated CCTO and CTO, along with a straddling type-I interfacial band gap. The conditions should differ in the case of defective materials; this is because of the segregation of point defects, as well as lattice distortion at the heterostructure interface or surface. As shown in Fig. 4(a), the electronic transitions are associated with the cubic CCTO phase (2.20 eV and 2.50 eV) and orthorhombic CTO phase (3.24 eV and 3.53 eV). The theoretically calculated E_{gap} values are greater than the experimentally obtained values, which, in principle, can indicate a high concentration of structural defects. This leads to the formation of intermediate levels between the valence (VB) and conduction (CB) bands of these composites, which is largely responsible for the reduction of the E_{gap} values. Moreover, our results suggest that an extended milling period tends to have a positive effect on the crystallization process of such systems. To investigate the crystalline structure of the mixed-phase CCTO/CTO composite powders at medium-range, we also performed PL emission measurements at room temperature, as shown in Fig. 4(b). These composites exhibit a broad PL emission band with a maximum intensity at 450 nm. The enhanced crystalline quality (owing to the longer milling period) results in an improved electronic configuration. This is especially evident at medium-range, and promotes an increase in the relative intensity of the PL emission band, accompanied by its enlargement (see Fig. 4(b)). In theory, owing to the PL behavior of the CCTO/CTO composite, certain localized states should exist in the forbidden band gap, which is typical of the multiphonon process [28,29].

Based on previous experimental and theoretical findings [45–47], it is presumed that structural order–disorder effects can, in theory, facilitate the population of electronic excited states, and hence promote an intense PL emission band in the case of such complex materials. This theory corresponds with the structural and optical properties that were observed for the CCTO/CTO composite. Furthermore, it is important to investigate the role of the structural changes that occur during the synthesis of these complex materials; in particular, it is important to determine how the building blocks are organized at the short-, medium- and long-ranges of the crystalline structure to elucidate the behavior and properties at nanoscale, as well as provide important insights on the structure–property relationships. It is possible that the PL behavior can, in theory, be explained in terms of the structural and electronic order–disorder effects at the interfacial regions of the CCTO/CTO.

From the viewpoints of theoretical and computational materials design, in principle, provide a detailed understand the materials properties in term of their structure, as well as, reveals important aspects of their physical and chemical behavior at the atomic level [45–49]. In particular, in the CTO unit cell, the Ca atoms are coordinated to twelve O atoms that form dodecahedral [CaO_{12}] clusters while the Ti atoms are coordinated to six O atoms that form octahedral [TiO_6] clusters. However, in addition to these complex clusters, the CCTO unit cell also possesses Cu atoms, which are coordinated to four O atoms that form square planar [CuO_4] cluster (see Fig. 5(a)) [28,29]. To further clarify the PL mechanism, the structural changes observed in this study suggest that these complex clusters are highly disordered at the interfaces of both materials. Our results suggest that cooperative effects occur at the short-, medium- and long-ranges of these complex clusters; these effects primarily occur at the interface regions of the CCTO/CTO composites and thus are responsible for the modification of their physical and chemical behavior at nanoscale.

An analysis of the DOS, displayed in Fig. 5(b), shows the contribution of the Cu [Ar] $3d^9$ levels to the ferromagnetic solution

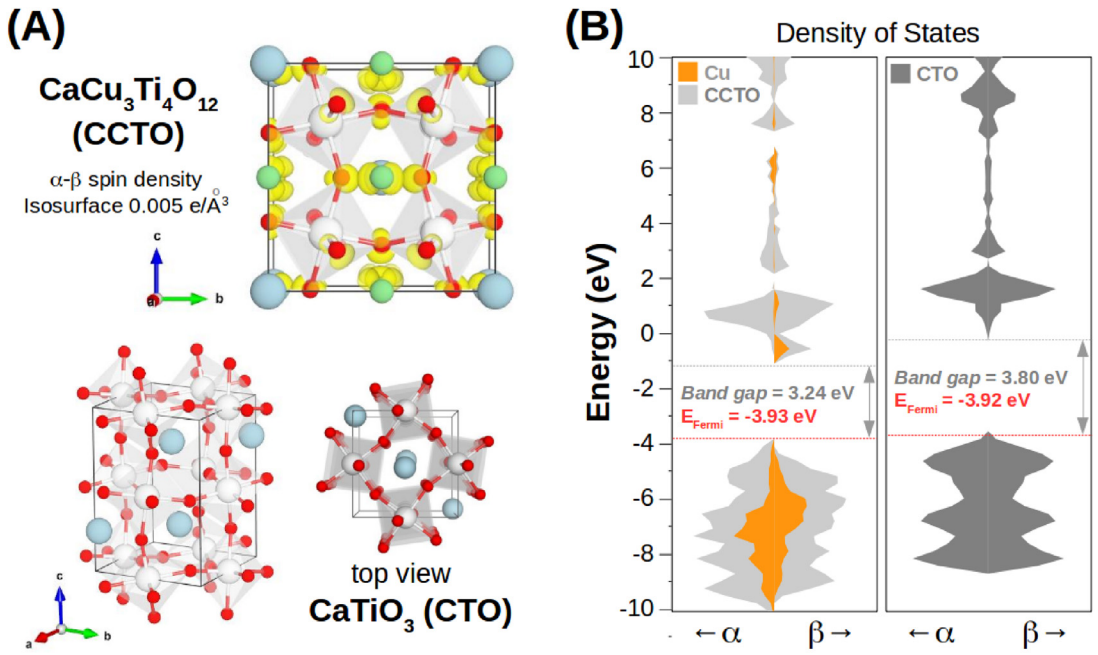

Fig. 5. (a) Unit cells of CCTO, with its ferromagnetic spin density isosurface (in yellow), and CTO cell. The Cu, Ca, Ti, O ions are shown in green, light blue, white and red colors, respectively. The bent [TiO_6] polyhedral in both cases are indicated in light grey. (b) Density of states of CCTO and CTO at the HSE06 with its Fermi level and band alignment. The assimetry of spin up and spin down electrons in the ferromagnetic CCTO is created by the Cu ([Ar]$3^{10}4s^1$) atoms. The Cu partial DOS is shown in orange color, occupying the bottom of conduction band. (For interpretation of the references to colour in this figure legend, the reader is referred to the web version of this article.)

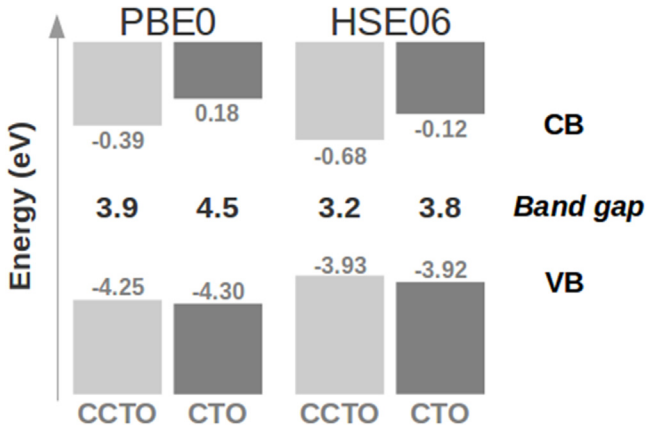

Fig. 6. Band alignment of CCTO and CTO at several hybrid functionals. The top of valence band is almost degenerate in all cases, while the bottom of conduction band of CTO is higher in energy than CCTO, leading to a band gap energy difference about 0.7 eV.

(first triplet ground state) at the edge of both VB and CB bands, along with the contribution of the O 2p levels at the VB and that of the Ti 3d level at the CB. In the case of the CTO, the absence of Cu cations led to the singlet ground state solution, where the top of the VB is composed of O 2p levels and the bottom of the CB is primarily composed of antibonding Ti 3d levels.

Fig. 6 illustrates an electronic model based on a theoretical perspective, which can be used to predict the band-gap alignment of the CCTO/CTO composite. It is noteworthy that the theoretical model used here is based on the band alignments of both the CCTO and CTO materials, which are considered separately; it therefore fails to consider some key factors, such as the complex chemical interactions that occur during the formation of the composite system, as well as the effect of interfacial strain [31,50,51]. However, in principle, the computational strategy used here can be used to elucidate a number of relevant effects, with the aim of exploring the physical and chemical behavior of these composites at an atomic level. Overall, in the case of these composites, the electron-hole pair formation is strongly connected to the energy level alignment. From a computational perspective, the method using the PBE0 functional is expected to result in a larger band gap compared with that of the range-separated HSE06 functional because of its significantly high Hartree–Fock contribution. The qualitative results correlate with the trends shown by the experimental results and the time-consuming HSE06 method. In addition, we also investigated the gas-sensing properties of the CCTO/CTO thick films (see Fig. 7(a–d)).

Fig. 7(a–d) shows the resistance plotted as a function of time for the CCTO/CTO thick films that were subjected to air and CO atmospheres at 390 °C, respectively. It can be observed that the corresponding curves of the CCTO/CTO thick films exhibit typical n-type semiconductor behavior. When exposed to an air atmosphere, the resistance of the CCTO/CTO_1 film rapidly increases (see Fig. 7(a)).

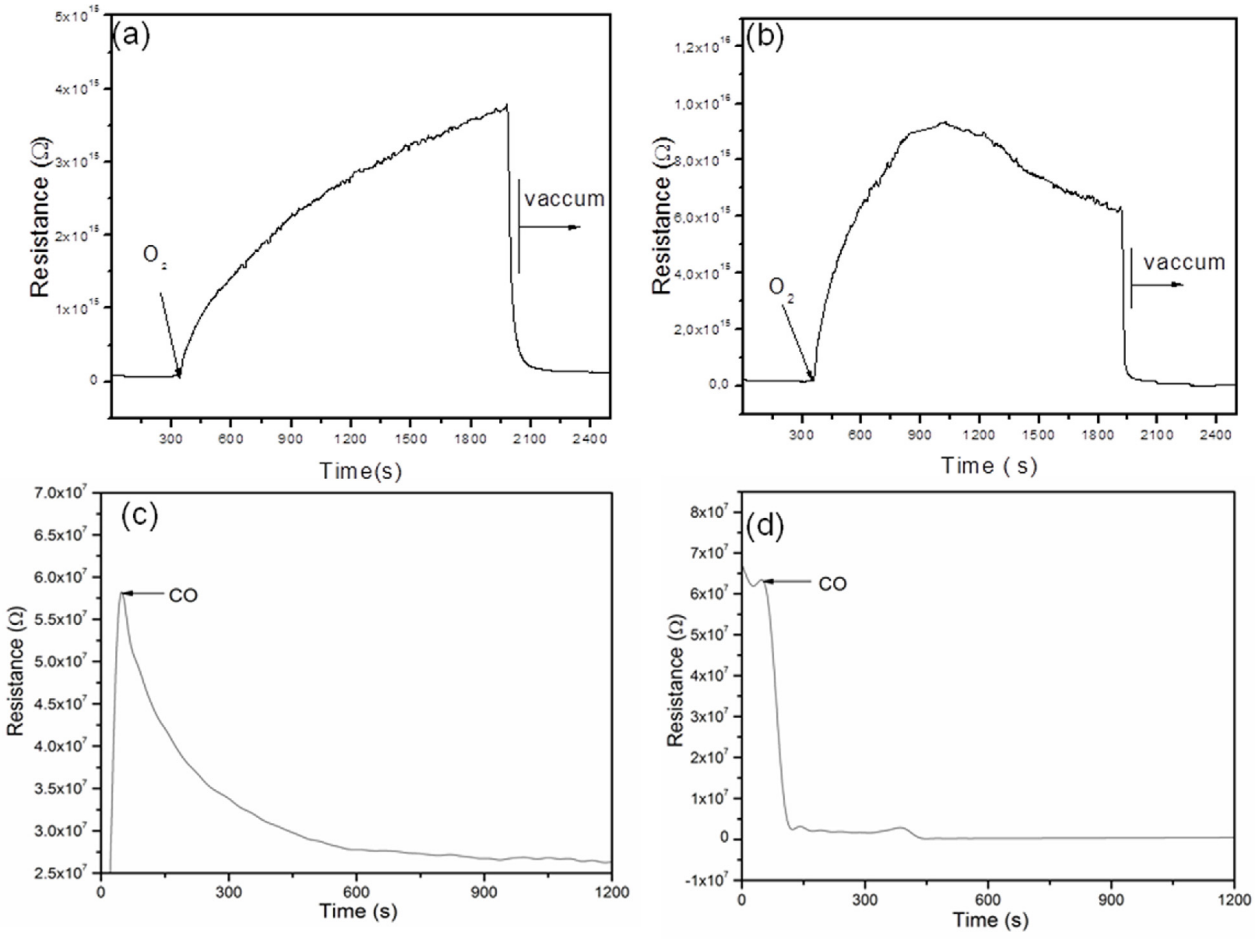

Fig. 7. Resistance vs time curves at 400°C of the CCTO/CTO_1(a), CCTO/CTO_2(b) thick films under air atmosphere and CCTO/CTO_1(c) and CCTO/CTO_2 (d) thick films under CO atmosphere.

By considering the complex cluster notation, we can determine that the interaction between the oxygen and grain surface promotes electron transfer between the $[TiO_5V_O^{\bullet}]$,$[CaO_{11}V_O^{\bullet}]$ and $[CuO_4]^x$ to oxygen from the air atmosphere. In addition, the possible energy-transfer process between the clusters in the lattices of the CCTO/CTO systems can be ascribed to order–disorder effects according to the following equations:

$$[TiO_5V_O^{\bullet}] + O_2 \rightarrow [TiO_5V_O^{\bullet\bullet}] \cdots O_2^{'}(ads) \quad (3)$$

$$[CaO_{11}V_O^{\bullet}] + O_2 \rightarrow [CaO_{11}V_O^{\bullet\bullet}] \cdots O_2^{'}(ads) \quad (4)$$

$$[CuO_4]^x + O_2 \rightarrow [CuO_4]^{\bullet} \cdots O_2^{'}(ads) \quad (5)$$

Consequently, the sample resistance increases because there is an increase in the both the barrier height and depletion width [52]. In particular, the resistance stabilization period (i.e., the response time) for this sample was prolonged, which is related to its small surface area and aggregated particles. The resistance stabilization period for the CCTO/CTO_2 film was also prolonged; however, a decrease in the resistance rather than stabilization was noted (see Fig. 7(b)). This behavior is attributed to oxygen adsorption at the surface, which favors electron transference from O_2 to clusters, reduces the concentration of oxygen vacancies and overlaps the potential barriers. Therefore, the conductivity of this sample decreases according to the following equations:

$$[TiO_5V_O^{x}] + O_2 \rightarrow [TiO_5V_O^{\bullet}] \cdots O_2^{'}(ads) \quad (6)$$

$$[CaO_{11}V_O^{x}] + O_2 \rightarrow [CaO_{11}V_O^{\bullet}] \cdots O_2^{'}(ads) \quad (7)$$

$$[TiO_5V_O^{\bullet}] \cdots O_2^{'}(ads) \rightarrow [TiO_6]^x + \tfrac{1}{2}O_2 \quad (8)$$

$$[CaO_{11}V_O^{\bullet}] \cdots O_2^{'}(ads) \rightarrow [CaO_{12}]^x + \tfrac{1}{2}O_2 \quad (9)$$

When thick films are exposed to CO gas, three processes may occur: (i) CO adsorption at the surface, which correlates with the enhancement of the potential barrier height as well as the conductivity values; (ii) the CO reacts with the O_2 that is adsorbed on the surface, in accordance with Eqs. (10) and (11) below, and (iii) oxygen vacancies act as electron donors, which also increases the conductivity of the film. In good agreement with previous works [53,54], we would expect that the relevant reactions are the following.

$$[TiO_5V_O^{\bullet}] \cdots O_2^{'}(ads) + CO_{(g)} \rightarrow [TiO_6]^x + CO_2 + \tfrac{1}{2}O_2 \quad (10)$$

$$[CaO_{11}V_O^{\bullet}] \cdots O_2^{'}(ads) + CO_{(g)} \rightarrow [CaO_{12}]^x + CO_2 + \tfrac{1}{2}O_2 \quad (11)$$

Fig. 7(c) and (d) show the resistance versus time curves that were recorded for the CCTO/CTO_1 and CCTO/CTO_2 thick films, respectively. Owing to the high degree of connectivity between the particles, oxygen diffusion not only occurs at the surface of the aggregates but also throughout the material [52,55].

Table 1
Sensitivity values to a dry air atmosphere, $S = R_{air}/R_{vacuum}$, obtained by means of CO assays for CCTO/CTO thick films at 390 °C.

Sample	Sensitivity P_{air} = 3.6 mmHg	Sensitivity P_{air} = 9.0 mmHg
CCTO/CTO_1	3.5	6.2
CCTO/CTO_2	27.1	46.4

Table 2
Sensitivity values to a CO atmosphere, $S1 = R_{CO}/R_{vacuum}$ and $S2 = R_{air+CO}/R_{air}$, obtained by means of CO assays for CCTO/CTO thick films at 390 °C.

Sample	S1	S2
CCTO/CTO_1	2.30	1.29
CCTO/CTO_2	80.00	86.00

Table 1 illustrates the sensitivity values ($S = R_{air}/R_{vacuum}$) of the samples that were remained under vacuum and, after resistance stabilization, they were subjected to a dry air atmosphere at a pressure of 3.6 and 9.0 mmHg. Maximum electrical sensitivity values were obtained for the sample that was subjected to a pressure of 9.0 mmHg at 390 °C. The sensitivity of the samples increased with the air pressure. The highest electrical sensitivity was determined for the CCTO/CTO_2 thick film. This film contained a large quantity of aggregated particles because of its large surface area; in addition, the degree of disorder of the lattice was high, which can probably be attributed to the presence of oxygen vacancies.

For the analysis of the sensitivity values of the samples to a CO atmosphere, two assays were conducted. Firstly, samples were remained under vacuum conditions and were subjected to a CO-rich atmosphere (S1 assay), and secondly, samples exposed to a O_2-rich atmosphere and subsequently exposed to a CO atmosphere (S2 assay). The S1 index represents the calculated sensibility values of the samples that were exposed to a CO atmosphere at a pressure of 3.6 mmHg, and the S2 index represents the calculated sensibility of the samples that were exposed to an atmosphere of CO ($P_{air} + P_{CO}$) at a pressure of 20 mmHg, and the results are listed in Table 2.

The results in Table 2 confirm that the samples that remained under vacuum conditions and were subjected to a CO-rich atmosphere (S1 assay) had a superior response to those of the S2 assay for sample CCTO/CTO_1. When the CCTO/CTO_1 thick film was exposed to a O_2-rich atmosphere and subsequently exposed to a CO atmosphere, there was an apparent decrease in the sensibility values. This behavior can be attributed to the reaction between the CO gas and the exposed surface of the thick film. Finally, the CCTO/CTO_2 thick film had a better response in both assays which can be related the microstructural and structural characteristics and the possible previous overlapping of the potential barriers [52].

4. Conclusion

In summary, CCTO/CTO systems were prepared by a solid-state reaction with 24 h or 48 h of grinding. The XRD patterns and Rietveld refinement results showed that the CCTO/CTO composite systems are composed of a cubic CCTO phase and an orthorhombic CTO phase. The MR spectroscopy results indicated that the symmetry break along the Ti-O linkages is due to the existence of structural defects, such as distortions and strains in the CCTO/CTO systems, which were induced by the milling stages. The DRS/UV-vis spectra showed that these structural defects in the crystalline structure inhibited the energy levels between the CBs and VBs. The FE-SEM micrographs showed that the CCTO/CTO powders and thick films are composed of aggregated particles, and the heat treatment that was conducted at 500 °C influenced the conductivity between the particles of the CCTO/CTO thick films. The electrical measurements that were recorded under oxygen (from dry air atmosphere) and CO atmospheres confirmed that the electron transference to/from the oxygen or CO influenced the resistance and sensibility values. The CCTO/CTO_2 film exhibited a good sensing response under the experimental conditions employed. In general, the high PL emission and sensor response

of these composites can, in principle, be attributed to the effective band alignment of the CCTO/CTO composite. Specifically, the electron–hole pair formation is strongly connected to the energy-level alignment.

Acknowledgements

This work was supported by Brazilian agencies: FAPESP (2013/07296-2; 2016/07476-9), CNPq (573636/2008-7) and CAPES/PROCAD. The computational facilities were supported by resources supplied by Molecular Simulations Laboratory, São Paulo State University, Bauru, Brazil.

Appendix A. Supplementary data

Supplementary data associated with this article can be found, in the online version, at http://dx.doi.org/10.1016/j.materresbull.2017.04.037.

References

[1] M.A. Subramanian, D. Li, N. Duan, B.A. Reisner, A.W. Sleight, J. Solid State Chem. 151 (2000) 323–325.
[2] K.S. Aleksandrov, B.V. Beznosikov, Crystallogr. Rep. 52 (2007) 28–36.
[3] S.M. Moussa, B.J. Kennedy, Mater. Res. Bull. 36 (2001) 2525–2529.
[4] A.N. Vasil'ev, O.S. Volkova, J. Low Temp. Phys 33 (2007) 895–914.
[5] S.Y. Chung, I.D. Kim, S.J.L. Kang, Nat. Mater. 3 (2004) 774–778.
[6] A.P. Ramirez, M.A. Subramanian, M. Gardel, G. Blumberg, D. Li, T. Vogt, S.M. Shapiro, Solid State Commun. 115 (2000) 217–220.
[7] C.C. Homes, T. Vogt, S.M. Shapiro, S. Wakimoto, A.P. Ramirez, Science 293 (2001) 673–676.
[8] A.P. Litvichuk, C.L. Chen, N. Kolev, V.N. Popov, V.G. Hadjiev, Phys. Status Solidi A 195 (2003) 453.
[9] M.H. Cohen, J.B. Neaton, L. He, D.V. Vanderbilt, J. Appl. Phys. 94 (2003) 3299.
[10] D.C. Sinclair, T.B. Adams, F.D. Morrison, A.R. West, Appl. Phys. Lett. 80 (2002) 2153–2155.
[11] T.T. Fang, C.P. Liu, Chem. Mater. 17 (2005) 5167–5171.
[12] T.T. Fang, L.T. Mei, H.F. Ho, Act. Mater. 54 (2006) 2867–2875.
[13] D. Capsoni, M. Binia, V. Massarottia, G. Chiodelli, M.C. Mozzatic, C.B. Azzonic, J. Sol. State Chem. 177 (2004) 4494–4500.
[14] K.M. Kim, J.H. Lee, K.M. Lee, D.Y. Kim, D.H. Riu, S.B. Lee, Mater. Res. Bull 43 (2008) 284–291.
[15] M.A. Ramírez, P.R. Bueno, R. Tararam, A.A. Cavalheiro, E. Longo, J.A. Varela, J. Phys. D: Appl. Phys. 42 (2009) 185503.
[16] A.O. Turky, M.M. Rashad, Z.I. Zaki, I.A. Ibrahim, M. Bechelany, RSC Adv. 5 (2015) 18767–18772.
[17] J.-C. Zheng, A.I. Frenkel, L. Wu, J. Hanson, W. Ku, E.S. Božin, S.J.L. Billinge, Y. Zhu, Phys. Rev. B 81 (2010) 144203.
[18] R.L. Nigro, R.G. Toro, G. Malandrino, I.L. Fragalá, P. Fiorenza, V. Raineri, Thin Solid Films 515 (2007) 6470.
[19] M. Sato, R. Tu, T. Goto, Materi. Trans. 47 (2006) 1386–1390.
[20] L. Feng, Y. Wang, Y. Yan, G. Cao, Z. Jiao, J. Appl. Surf. Sci. 253 (2006) 2268.
[21] R. Jimenez, M.L. Calzada, I. Bretos, J.C. Goes, A.S.B. Sombra, J. Eur. Ceram. Soc. 27 (2007) 3829.
[22] M.A. Ramirez, A.Z. Simões, A.A. Felix, R. Tararam, E. Longo, J.A. Varela, J. Alloy Compd. 509 (2011) 9930–9933.
[23] Y. Lin, Y.B. Chen, T. Garret, S.W. Liu, C.L. Chen, L. Chen, R.P. Bontchev, A. Jacobson, J.C. Jiang, E.I. Maletis, J. Horwitz, H.D. Wu, Appl. Phys. Lett. 81 (2002) 631.
[24] T. Sequinel, I.G. Garcia, S.M. Tebcherani, E.T. Kubaski, L.H. Oliveira, M.S. Li, E. Longo, J.A. Varela, J. Alloys Compd. 583 (2014) 488–491.
[25] K. Fan, M. Liu, P. Tianyou, L. Maa, K. Dai, Renew. Energy 35 (2010) 555–561.
[26] L. Maa, M. Liu, P. Tianyou, K. Fan, L. Lua, K. Dai, Mat. Chem. Phys. 118 (2009) 477–483.
[27] B. Mahmoudia, N. Gabouze, M. Haddadi, B.R. Mahmoudia, H. Cheraga, K. Beldiilali, D. Dahmane, Sens. Actuators B 123 (2007) 680–684.
[28] L.H. Oliveira, E.C. Paris, W. Avansi, M.A. Ramirez, V.R. Mastelaro, E. Longo, J.A. Varela, J. Am. Ceram. Soc. 96 (2012) 209–217.
[29] L.H. Oliveira, A.P. de Moura, F.A. La Porta, I.C. Nogueira, E.C. Aguiar, T. Sequinel, I.L.V. Rosa, E. Longo, J.A. Varela, Mater. Res. Bull. 81 (2016) 1–9.
[30] C.M. Wang, S.Y. Lin, K.S. Kao, Y.C. Chen, S.C. Weng, J. Alloys Compd. 491 (2010) 423–430.
[31] N.L. Marana, F.A. La Porta, E. Longo, J.R. Sambrano, Curr. Phys. Chem. 5 (2015) 327–336.
[32] M.A. Ramirez, P.R. Bueno, J.A. Varela, E. Longo, Appl. Phys. Lett. 89 (2006) 212102.
[33] P.R. Bueno, W.C. Ribeiro, M.A. Ramírez, J.A. Varela, E. Longo, Appl. Phys. Lett. 90 (2007) 142912.
[34] M.A. Ramírez, P.R. Bueno, E. Longo, J.A. Varela, J. Phys. D: Appl. Phys. 41 (2008) 152004.
[35] P. Hohenberg, W. Kohn, Phys. Rev. 136 (1964) B864–B871.
[36] W. Kohn, L. Sham, J. Phys. Rev. 140 (1965) A1133–A1138.
[37] R. Dovesi, R. Orlando, A. Erba, C.M. Zicovich-Wilson, B. Civalleri, S. Casassa, L. Maschio, M. Ferrabone, M. De La Pierre, P. D'Arco, Y. Noel, M. Causa, M. Rerat, B. Kirtman, Int. J. Quantum Chem. 114 (2014) 1287.
[38] M.F. Peintinger, D.V. Oliveira, T. Bredow, J. Comput. Chem. 34 (2013) 451–459.
[39] A. Guinier, X-rays Diffraction in Crystals, Imperfect Crystals and Amorphous Bodies, W.H. Freeman, San Francisco, USA, 1963.
[40] D. Valim, A.G. Souza, P.T.C. Freire, S.B. Fagan, A.P. Ayala, J. Mendes, A.F.L. Almeida, P.B.A. Fechine, A.S.B. Sombra, J. Olsen, L. Gerward, Phys. Rev. B 70 (2004) 132103.
[41] N. Kolev, R.P. Bontchev, A.J. Jacobson, V.N. Popov, V.G. Hadjiev, A.P. Litvinchuk, M.N. Iliev, Phys. Rev. B 66 (2002) 132102.
[42] A.F.L. Almeida, R.S. de Oliveira, J.C. Goes, J.M. Sasaki, A.G. Souza, J. Mendes, A.S. B. Sombra, Mater. Sci. Eng. B. 96 (2002) 275–283.
[43] H. Zheng, G.D.C. Csete de Györgyfalva, R. Quimby, H. Bagshaw, R. Ubic, I.M. Reaney, J. Yarwood, J. Eur. Ceram. Soc. 23 (2003) 2653–2659.
[44] D.L. Wood, J. Tauc, Phys. Rev. B 5 (1972) 3144.
[45] L. Gracia, J. Andres, V.M. Longo, J.A. Varela, E. Longo, Chem. Phys. Lett. 493 (2010) 141–146.
[46] L. Gracia, V.M. Longo, L.S. Cavalcante, A. Beltran, W. Avansi, M.S. Li, V.R. Mastelaro, J.A. Varela, E. Longo, J. Andres, J. Appl. Phys. 110 (2011) 043501–043511.
[47] F.M.C. Batista, F.A. La Porta, L. Gracia, E. Cerdeiras, L. Mestres, M. Siu Li, N.C. Batista, J. Andrés, E. Longo, L.S. Cavalcante, J. Mol. Struct. 1081 (2015) 381–388.
[48] M.S. Pires, F.G.E. Nogueira, J.A. Torres, L.C.T. Lacerda, M.C. Pereira, T.C. Ramalho, RSC Adv. 6 (2016) 80830–80839.
[49] P.H. Ramos, F.A. La Porta, E.C. de Resende, J.O.S. Giacoppo, M.C. Guerreiro, T.C. Ramalho, Z. anorg, allg. Chem. 641 (2015) 780–785.
[50] Z. Zhang, J.T. Yates, Chem. Rev 112 (2012) 5520.
[51] L.A. Burton, A. Walsh, Appl. Phys. Lett 102 (2013) 132111.
[52] M.A. Ponce, C.M. Aldao, M.S. Castro, J. Eur. Cer. Soc. 23 (2003) 2105–2111.
[53] M. Batzill, U. Diebold, Prog. Surf. Sci. 79 (2005) 47–154.
[54] M.A. Ponce, M.A. Ramirez, F. Schipani, E. Joanni, J.P. Tomba, M.S. Castro, J. Eur. Ceram. Soc. 35 (2015) 153–161.
[55] C.M. Aldao, D.A. Mirabella, M.A. Ponce, A. Gilberti, C. Malagù, J. Appl. Phys 109 (2011) 063723.